Simulation and Experimental Analysis of the Temperature Field of Jet Flow of Aircraft Based on CFD Theory

ZHENGLEI CHEN, WANTONG CAI, LIANGCAI CAI, GUOPING CEN, AND HAIFU WANG

Department of Airport Construction Engineering, Air Force Engineering University, Xi'an 710038, China

Corresponding author: Zhenglei Chen (czl1126988739@163.com)

ABSTRACT As a key indicator of airport concrete pavement, the durability of concrete is seriously affected by the jet flow generated by aircraft engines. In order to clarify the temperature field distribution of aircraft jet flow acting on the pavement surface, this paper obtained the temperature field distribution of pavement surface under the action of three types of aircraft jet flow by combining field test experiment and CFD simulation. CFD simulation adopts the shear stress transfer model which is often used in engineering problem calculation, and the field test experiment adopts the method of embedding temperature sensor in precast concrete slab. The paired two sample t test was used to test the difference between the experimental results and the simulation results. The experimental results show that the pavement temperature increases first and then decreases with the distance from the engine, and reaches the maximum at the intersection point of the jet flow and the airport pavement. The simulation curve is in good agreement with the experimental results. When the level of confidence is 0.01, there is no significant difference between the simulation value and the experimental value, which verifies the accuracy and feasibility of the simulation calculation model. The simulation results of the three aircraft showed that when type C aircraft is in the state of full afterforce, the maximum pavement temperature is the highest which is 22m away from the nozzle, and can reach 533.81K. The current work provides a new method for measuring the temperature distribution of airfield pavement under the action of jet flow and a basis for the application of fiber concrete in airfield pavement.

INDEX TERMS Jet flow, pavement, CFD, test experiment, temperature field distribution.

I. INTRODUCTION

With the development of aviation industry, the number of flights increases year by year. In 2018, China's transport airlines completed 11.5352 million transport flight hours, an increase of 8.9 percent over the previous year.Transport airlines completed 4,694,700 flights, an increase of 7.6% over the previous year.The passenger transport volume of the whole industry reached 611,737,700, an increase of 10.9% over the previous year.The total volume of freight and mail transportation reached 7.3851 million tons, an increase of 4.6% over the previous year [1]. The continuous growth of aviation traffic has put forward higher requirements for the strength and durability of airport pavement. The development and promotion of new pavement materials with great strength

The associate editor coordinating the review of this manuscript and approving it for publication was Fabrizio Messina.

and durability have become a research hotspot. At present, fiber concrete technology [2], [3] is gradually developed and popularized in various fields. Compared with ordinary concrete, fiber concrete has better mechanical properties and durability, and its application in pavement field can effectively improve the service life of pavement.

Chen *et al.* [4] studied and prepared modified polyester synthetic fiber concrete, monofilament polypropylene synthetic fiber concrete, reticular polypropylene synthetic fiber concrete and polyacrylonitrile synthetic fiber concrete.The mechanical properties, durability and cost-effectiveness of fiber reinforced concrete are also studied. The results show that fiber reinforced concrete has great economic benefits in the field of airport pavement. From the perspective of absorption and release of strain energy, Wang *et al.* [5] studied the effect of steel fiber on the mechanical and deformation properties of concrete under thermal-force coupling.

IEEE Access

Z. Chen *et al.*: Simulation and Experimental Analysis of the Temperature Field of Jet Flow of Aircraft Based on CFD Theory

The results show that the compressive strength and the residual ratio of compressive strength can be effectively increased after steel fiber is mixed into concrete, the thermal expansion deformation of concrete can be restrained, and the absorption and release of strain energy of concrete can be improved. Generally speaking, there are few researches on the adaptability of fiber reinforced concrete in the field of airport pavement, which leads to some blindness in the promotion of fiber reinforced concrete in this field.

Given that most modern aircraft are powered by jet engines, during taxiing or test runs, the aircraft will generate high temperature jet currents that will act on the surface of the pavement for a long period of time. This will have a certain impact on the durability of airport pavement concrete. To promote the use of fiber concrete in the field of airport pavement, we must ensure that its durability can meet the needs of aircraft without causing excessive performance waste.Therefore, studying the temperature field distribution in the contact zone of the high-temperature jet flow in the pavement and mastering the maximum temperature under the jet flow of the aircraft are the key issues to be solved in the design and management of the pavement. It is of profound significance for study on the durability of airport pavement fiber concrete, the selection of pavement materials and airport daily maintenance management.

At present, the technology of using sensors to measure the surface properties has been very mature, and relevant scholars have carried out relevant studies on the physical properties, mechanical properties [6] and damage detection [7], [8] of the surface by means of sensors. In terms of the performance of measuring the surface temperature, Godoy *et al.* [9] designed a pavement temperature monitoring system using low-cost wireless temperature sensors to monitor the pavement temperature, and verified the feasibility of using sensors to measure the surface temperature.However, the signal of the wireless sensor gradually weakens with the increase of the surface depth, resulting in the error increasing with the increase of the pavement depth. Based on the sensor, Teltayev and Suppes [10] measured the temperature and humidity performance of the pavement surface, and analyzed the variation characteristics of the temperature of each pavement layer with time and the distribution of temperature at different moments on the depth. Cai *et al.* [11] designed an intelligent sensor network structure to measure the surface structure temperature, and verified the effectiveness and reliability of the system through experiments. The above research provides an idea for us to measure the temperature field distribution on the pavement under the action of jet flow.

The result obtained by field measurement is accurate, but it is expensive.With the development of computer industry, computational fluid dynamics [12], [13], as a simulation method for studying jet flow, has developed rapidly, and the method of computer simulation for calculating the temperature field distribution under the action of tailjet flow has been realized. Wang *et al.* [14] have conducted an experimental study on the exhaust flow field of a jet engine with

CFD method, and the results show that the pressure and temperature of the jet center decreased gradually with the increase of the distance from the jet to the nozzle. Benderskiy *et al.* [15], [16] using the RANS/ILES method, have simulated the jet flow of a double-cone supersonic aircraft, detected the influence of co-flow velocity and distance on temperature, pressure fluctuation and axial velocity in the jet hazard area, and studied the influence of natural wind speed on the jet hazard area. Yue *et al.* [17], [18] based on CFD theory and using the standard k-erm equation and three-dimensional n-s equation, have conducted numerical simulation of the jet impact on the flight deck and deflector during the takeoff of the carrier aircraft, and obtained the temperature characteristic distribution on the axis. Song *et al.* [19] have established a simulation model of jet flow of a carrier-borne aircraft, studied the influence of high temperature, high speed and high pressure jet flows on the guide plate under different deflection angles, and compared the simulation results with the experimental results. Liu *et al.* [20], [21] have studied the impact of a typical aircraft carrier deck and jet blast deflector (JBD) under the condition of under-expansion air flow with finite element method. Sun *et al.* [22] have analyzed the influence of jet flow of a carrier on the wind field, velocity field and pressure field on the deck based on the theory of computational fluid dynamics. The above research shows that both the field measurement experiment based on temperature sensor and the simulation based on computer can obtain the temperature field distribution of the airport pavement.In comparison, the data obtained from field measurement are accurate but the experiment cycle is long and the cost is high.The data obtained by the simulation is easy to operate but the data accuracy needs to be further tested.

Based on CFD theory, this paper established a numerical simulation model on the temperature field distribution of the pavement with the action of the jet flow.The field test of aircraft jet flow impact on pavement was designed and carried out, and the experimental results were compared with the numerical simulation results to further verify the accuracy of the numerical simulation method. On this basis, the temperature field distribution under the action of two other typical aircraft is analyzed numerically.Through comparative analysis of the influence of jet flow of three different aircraft types on the surface temperature field, the maximum temperature under the action of the jet flow is obtained. It is hoped to provide the basis for further research on the adaptability of fiber concrete in pavement and the durability of fiber concrete under the action of jet flow.

II. SIMULATION
A. THEORETICAL BASIS
With the rapid development of computer computing speed, numerical algorithms that use computers to accurately solve physical problems have also been developed rapidly. In the field of fluid mechanics. Computational fluid dynamics (CFD) is developed by combining theoretical fluid

Z. Chen *et al.*: Simulation and Experimental Analysis of the Temperature Field of Jet Flow of Aircraft Based on CFD Theory

IEEE *Access*

mechanics with experimental fluid mechanics, which provides a new idea for us to study the influence of various engine jet flows on airport pavement.

Computational fluid dynamics can express the characteristics of the flow field in the form of mathematical equations. By using three-dimensional rectangular coordinate system, the conserved N-S (Navier-Stokes) governing equations can be expressed as follows:

Fluid continuity equation:

$$\frac{\partial \rho}{\partial t} + \nabla \cdot (\rho \overrightarrow{W}) = 0 \tag{1}$$

Fluid motion equation:

$$\frac{\partial \rho \overrightarrow{W}}{\partial t} + \nabla \cdot (\rho \overrightarrow{W} \otimes \overrightarrow{W} + p[I])$$
$$- \nabla \cdot ([\tau]) + \rho \left(2\overrightarrow{\omega} \times \overrightarrow{W} + \overrightarrow{\omega} \times (\overrightarrow{\omega} \times \overrightarrow{r}) \right) = 0 \tag{2}$$

Fluid energy equation:

$$\frac{\partial \rho E}{\partial t} + \nabla \cdot (\rho E \overrightarrow{W} + p[I] \cdot \overrightarrow{W})$$
$$- \nabla \cdot (\kappa \nabla T + [\tau] \cdot \overrightarrow{W}) - \rho \nabla \left(\frac{\omega^2 r^2}{2} \right) \cdot \overrightarrow{W} = 0 \tag{3}$$

where, ρ is the density of the fluid; $\overrightarrow{W}$ is the relative velocity vector of the fluid; p is the static pressure of the fluid; $[I]$ is the unit tensor of fluid; $[\tau]$ is the viscous stress tensor of the fluid; E is the total energy of the fluid; ω is the rotational angular velocity of the fluid; r is the corresponding vector radius; κ is the thermal conductivity of the fluid; T is the temperature of the fluid.

Among them:

$$E = e + |W|^2/2 \tag{4}$$

where: e is the internal energy of fluid.

When equations (1), (2) and (3) are time-homogenized, then the N-S governing equation transforms to the Reynolds average N-S system of equation, which contains an additional pulsating quantity. In this equation, the pulsating quantity is an unknown quantity. The turbulence model related to various pulsating quantity needs to be established with the help of experience, so that the equations can be closed and the analytical solution can be achieved.

The commonly used turbulence models include zero equation, one equation and two equations. The zero equation and one equation model are too simple to calculate turbulent fluid accurately. Therefore, the current fluid calculation mostly adopts the two-equation model. Two-equation turbulence models such as $\kappa - \varepsilon$, $\kappa - \omega$, SST (Shear Stress Transfer) and SAS-SST (The Scale-Adaptive Simulation based on SST turbulence model) are most widely used. This paper adopts the SST two-equation model which is widely used in engineering problem calculation.

$\kappa - \omega$ turbulence model is relatively sensitive to the change of initial parameters of free fluid. The SST two-equation model combines the $\kappa - \varepsilon$ turbulence model and the

$\kappa - \omega$ turbulence model through the mixed function F_1, and adopts the $\kappa - \omega$ turbulence model in the near flow field and the $\kappa - \varepsilon$ turbulence model in the far flow field. The advantages of the two models are effectively exploited. The specific description is as follows:

$$\frac{\partial (\rho \kappa)}{\partial t} + \frac{\partial \left(\rho u_j \kappa \right)}{\partial x_j}$$
$$= P_\kappa \left(\frac{M_\infty}{Re} \right) - \beta^* \rho \omega \kappa \left(\frac{Re}{M_\infty} \right)$$
$$+ \frac{\partial}{\partial x_j} [(\mu + \frac{\mu_T}{\sigma_x}) \frac{\partial \kappa}{\partial x_j}] \left(\frac{M_\infty}{Re} \right) \tag{5}$$

$$\frac{\partial (\rho \omega)}{\partial t} + \frac{\partial \left(\rho u_j \omega \right)}{\partial x_j}$$
$$= P_\omega \left(\frac{M_\infty}{Re} \right)$$
$$- \beta \rho \omega^2 \left(\frac{Re}{M_\infty} \right) + \frac{\partial}{\partial x_j} [(\mu + \frac{\mu_T}{\sigma_x}) \frac{\partial \omega}{\partial x_j}] \left(\frac{M_\infty}{Re} \right)$$
$$+ 2 (1 - F_1) \frac{\rho}{\sigma_{\omega 2} \omega} \frac{\partial \kappa}{\partial x_j} \frac{\partial \omega}{\partial x_j} \left(\frac{M_\infty}{Re} \right) \tag{6}$$

Mixed function F_1 is:

$$F_1 = \tanh \left(\Phi_1^4 \right) \tag{7}$$

Among them:

$$\Phi_1 = \min \left[\max \left(\frac{\sqrt{k}}{0.09 \omega y}, \frac{500 \mu}{\rho y^2 \omega} \right), \frac{4 \rho k}{1.168 D_\omega^+ y^2} \right] \tag{8}$$

$$D_\omega^+ = \max \left[2\rho \frac{1}{\sigma_{\omega,2}} \frac{1}{\omega} \frac{\partial k}{\partial x_j} \frac{\partial \omega}{\partial x_j}, 10^{-20} \right] \tag{9}$$

The eddy viscosity is expressed as:

$$\mu_T = \min \left[\frac{\rho \kappa}{\omega}, \frac{a_1 \rho \kappa}{SF_2} \left(\frac{Re}{M_\infty} \right) \right] \tag{10}$$

Among them:

$$F_2 = \tanh \left(\Phi_2^2 \right) \tag{11}$$

$$\Phi_2 = \max \left[2 \frac{\sqrt{k}}{0.09 \omega y}, \frac{500 \mu}{\rho y^2 \omega} \right] \tag{12}$$

Among them:

$$S = \sqrt{2 S_{ij} S_{ij}}, \quad S_{ij} = \frac{1}{2} (\frac{\partial \mu_i}{\partial x_j} + \frac{\partial \mu_j}{\partial x_i}) \circ$$

Reynolds stress is expressed as:

$$\tau_{ij} = 2\mu_T \left(S_{ij} - \frac{1}{3} \frac{\partial u_\kappa}{\partial x_k} \delta_{ij} \right) - \frac{2}{3} \rho \kappa \delta_{ij} \tag{13}$$

The approximate expression of the generation term of turbulent kinetic energy and specific dissipation rate is:

$$P_\kappa = \tau_{ij} \frac{\partial u_i}{\partial x_j} = \mu_T S^2 \tag{14}$$
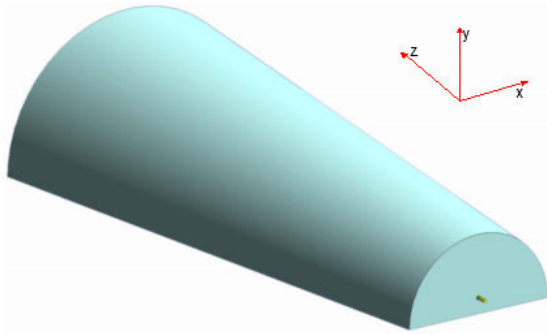
$$P_\omega = \frac{\gamma \rho P_\kappa}{\mu_T} \tag{15}$$

FIGURE 1. Schematic diagram of jet flow field calculation area.

FIGURE 2. Schematic diagram of type A aircraft engine nozzle model.

a. Grid of far field

b. Grid of nozzle outlet section

FIGURE 3. Schematic diagram of grid structure of calculation area.

B. GEOMETRIC MODEL

Geometric model forms the basis of numerical simulation calculation. The suitability and accuracy of the geometric model directly affect the results of numerical simulation calculation. In this paper, ICEM software is used to construct a geometric model. The problem studied in this paper is the influence of jet flow on the pavement temperature field, and the geometric entity is divided into two parts: a plane and pavement. In order to facilitate modeling and calculation, the aircraft model is simplified as the engine nozzle model, and the pavement model is replaced by the calculation area. Therefore, the geometric model is divided into two parts: the calculation area model and the engine nozzle model. Type A aircraft is selected to facilitate the comparison between numerical calculation results and field measurement results.

1) MODEL OF CALCULATION AREA

Considering that the jet flow from the engine of an aircraft touches the pavement soon after ejecting, the airflow diffusion is restricted by the constraint of pavement, which is taken into account when establishing the calculation model. In order to calculate the temperature field distribution in the far field, a near half circular truncated cone region is taken as the calculation area of the entire flow field. The length of this area is 75.00m. A semicircle with a radius of 5.00m is selected for the position of the airflow inlet, and a semicircle with a radius of 20.00m is selected for the position of the airflow outlet (see Fig. 1). Three-dimensional rectangular coordinate system is adopted for the simulation calculation. The flow direction along the engine airflow is positive along the Z axis, and the vertical direction is positive along the Y axis (positive up). The direction perpendicular to the flow direction and pointing to the right is positive along the X axis.

2) MODEL OF ENGINE NOZZLE

The aircraft for the numerical simulation calculation is type A aircraft. The engine nozzle of this type of aircraft is the ejector nozzle with a diameter of 0.53m and the lowest point of the nozzle is 1.10m above the ground. When the engine is working, the total temperature is 1178.15K, the static temperature is 1051.15K, and the airflow velocity at the outlet of the nozzle is 545m/s. According to the geometric parameters
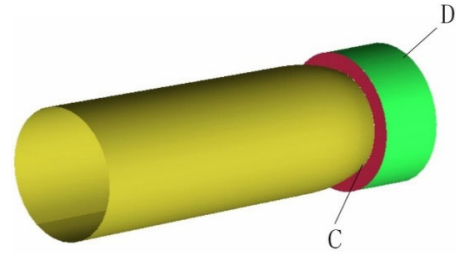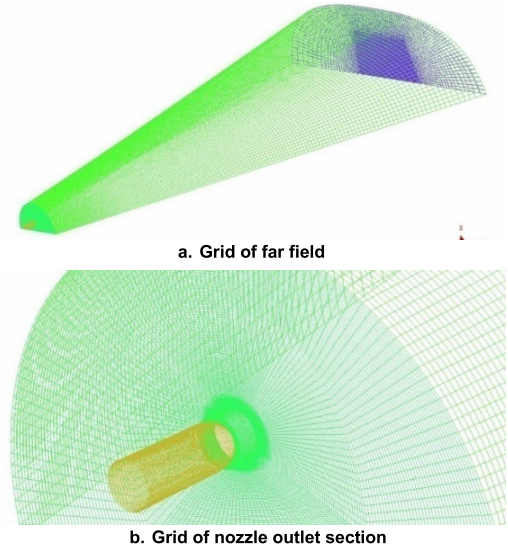
of the jet nozzle of the type A aircraft engine, the model of engine nozzle is simplified as shown in Fig. 2. Section C is the adjusting ring(see Fig. 2), which can be utilized to control the area of the main flow section of the ejector nozzle outlet. Section D is the secondary flow section of the ejector nozzle outlet. And this section has a certain influence on the diffusion of the airflow ejected from the nozzle. This model simplified it into an extensive section with a sudden change in sectional area at the outlet of the ejector nozzle.

C. GRID DIVISION
1) GRID DIVISION OF CALCULATION AREA

The partitioning method of network model and grid quality have great influence on the numerical simulation results. It is very important to reduce the number of grids and improve the accuracy and efficiency of computation by adopting reasonable meshing methods and using structured meshing as far as possible. The whole calculation area is divided into several sub-regions by the block grid method to generate grids (see Fig.3(a)). The internal, outlet and outlet cross section grids of the nozzle are partially encrypted(see Fig.3(b)).

2) GRID DIVISION OF ENGINE NOZZLE

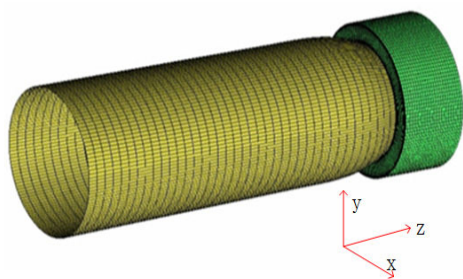Based on the above simplified model, the engine nozzle is meshed. Using ICEM CFD software and block subdivision

Z. Chen *et al.*: Simulation and Experimental Analysis of the Temperature Field of Jet Flow of Aircraft Based on CFD Theory

IEEE *Access*

FIGURE 4. Schematic diagram of engine nozzle grid structure.

TABLE 1. Maximum pavement temperature under different number of grids.

The grid number	3000000	5000000	7000000
The maximum temperature(K)	369.35	376.92	377.69

TABLE 2. Maximum pavement temperature at different time steps.

Time step(s)	0.005	0.001	0.0001
The maximum temperaturez(K)	372.63	376.92	375.21

method, the structural grid of engine nozzle is obtained as shown in Fig.4. The cross section of the nozzle is O-mesh and the axial direction is H-mesh.The three-dimensional rectangular coordinate system is also adopted. The origin of coordinates (0,0,0) is set at the center of the airflow outlet section of thet engine nozzle.

D. MODEL SOLUTION

The boundary conditions at the inlet of the calculated area were set as pressure inlet conditions, where the total temperature at the nozzle nozzle was 1200.00K, the total pressure was 1.34 atm, and the remaining positions were set as standard atmospheric conditions.The outlet boundary conditions were set as open boundary conditions, and the mean static pressure and mean temperature were set as standard atmospheric conditions. The pavement surface condition is set as adiabatic no slip wall.On this basis, the A-type aircraft is simulated numerically.

In order to solve the three dimensional Navier-Stokes equations in relative coordinate system. The finite volume method based on cell center is chosen as the difference method, and the implicit propulsion algorithm is used in the time advance method. The turbulence model is SST model, which uses standard $\kappa - \omega$ model in the region of low reynolds number inside the boundary layer, and $\kappa - \varepsilon$ model in the region of high reynolds number outside the boundary layer, so that the equation is suitable in the region of near field and the region of far field. In the governing equation, the convection term is discretized in the second-order upwind scheme, and the time integral is carried out by the second-order backward euler equation. The turbulence equation is solved by the first order upwind scheme and the turbulence variable is solved by the finite second order implicit euler equation.

In the calculation of this paper, the convergence conditions are as follows:

1) The total residual flow of the whole field is reduced to below 10^{-5};

2) The relative value of the residual flow of nozzle and inlet to the total residual flow of the whole field is less than 1%;

3) As the number of iteration steps increases, the total performance parameters no longer change significantly, and the parameters at a certain point in the flow field remain unchanged.

E. MODEL VALIDATION

1) GRID INDEPENDENCE TEST

The time step is set as 0.001s, and the three computational grids with 3 million, 5 million and 7 million grids are numerically calculated. When the surface temperature reached steady state, the maximum temperature of the surface is recorded(see Table 1).

As can be seen from the table, when the number of grids exceeds 5 million, there is little difference in the limit temperature of the surface.Finally, the total number of grids selected in this paper is 5 million, which can ensure the computing efficiency on the premise of satisfying the calculation accuracy.

2) TIME INDEPENDENCE TEST

The number of grids is set as 5 million, and 0.005s, 0.001s and 0.0001s are selected for the time step to test the time independence of the selected number of grids. After the simulation reaches steady state, the maximum temperature is recorded(see Table 2).

As can be seen from the table, when the number of grids is constant, the effect of time step on the limit temperature is not obvious. After comprehensive consideration, the time step of this paper is 0.001s

F. RESULT ANALYSIS

Fig.5 is the cloud diagram of temperature distribution on the pavement with the act of the jet flow from the engine. From the analysis in Fig. 5, it can be seen that, from the horizontal perspective, the surface temperature presents a trend of symmetric decrease from the central axis to both sides, and finally approaches the ambient temperature. From the perspective of the axial direction, the surface temperature of the pavement show a trend of first rising and then falling under the action of the jet flow, and the width of the high temperature area begins to decrease after increasing to a certain width. Fig. 6 shows the surface temperature change curve of the central axis. As can be seen from the figure, the surface temperature of the pavement begins to rise from 7.00m away from the outlet of the nozzle along the Z axis, and reaches the highest temperature in the region of 12.00m~28.00m and the peak value at 17.00m. Then, as the distance from the
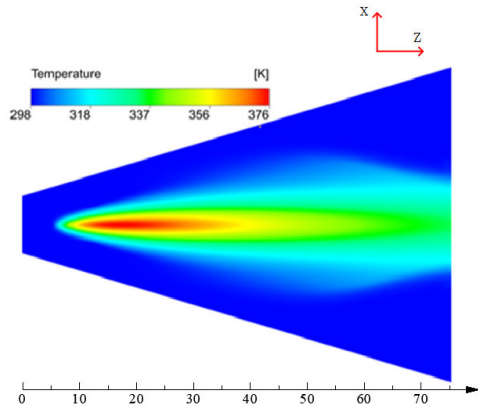
IEEE *Access*

Z. Chen *et al.*: Simulation and Experimental Analysis of the Temperature Field of Jet Flow of Aircraft Based on CFD Theory

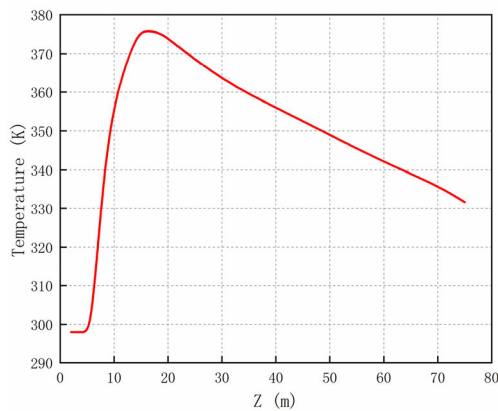**FIGURE 5.** Surface temperature distribution cloud diagram of the pavement.

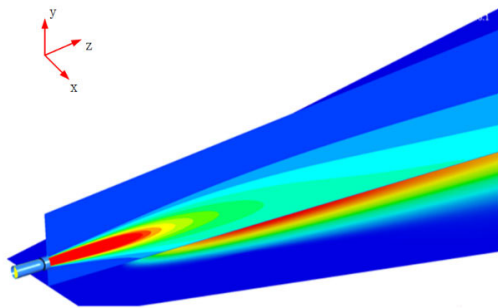**FIGURE 6.** Temperature curve of central axis of surface of the pavement (X=0).

FIGURE 7. Schematic diagram of the influence of the jet on the surface temperature of the pavement.

nozzle increases, the airflow temperature on the surface of the pavement gradually decreases and finally approaches the ambient temperature. Fig. 7 is a schematic diagram of the influence of the jet flow on the pavement temperature.

III. FIELD MEASUREMENT EXPERIMENT
In order to further verify the accuracy of temperature field distribution under the action of jet flow, field experiment was carried out at an airport in shaanxi province, China. Type A

FIGURE 8. Site layout of precast concrete slab.

aircraft directly jets the flow to the pavement under the afterforce state. After the temperature was stable, the temperature of different positions on the pavement was measured, and the experimental results and numerical simulation results were compared to verify the feasibility of the simulation model.

A. EXPERIMENTAL PREPARATION
The instruments used in this experiment include infrared thermometer, temperature sensor, temperature converter and data acquisition device. Among them, the infrared thermometer adopts smart sensor AS530 handheld infrared thermometer with a measuring range of -32~550° to determine the approximate position of the peak temperature point of the pavement. The data acquisition device adopts the DAM-3055 data acquisition card produced by altai technology to collect the temperature data measured by the sensor. This experiment adopts type A aircraft with the engine nozzle height of 1.36m and engine installation Angle of 5°.

The pavement was replaced by cement concrete slab. In order to facilitate the measurement data, precast concrete slab was cast in advance for embedding temperature sensors and temperature converters. In order to facilitate transportation and experiment laying, the size of the concrete slab was set as 0.50m×0.50m×0.05m and the weight is about 30Kg. According to the experimental needs, 42 concrete slabs were poured in total. The layout range was 4.50m long and 2.50m wide. The site layout was shown in Fig.8.

B. ARRANGEMENT OF MEASURING POINTS
According to the study of Feng *et al.* [23] it is known that the contact point of jet flow and pavement has the highest temperature.Therefore, before the experiment, it is necessary to determine the contact point between the jet flow and the pavement. Aircraft engine installation is generally not parallel to the ground, but into a certain angle, which is called engine installation angle, as shown in Fig.9. Due to the installation angle, the jet flow from the aircraft always
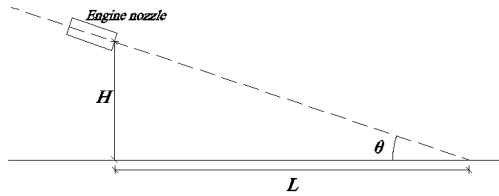
Z. Chen *et al.*: Simulation and Experimental Analysis of the Temperature Field of Jet Flow of Aircraft Based on CFD Theory

IEEE *Access*

FIGURE 9. Schematic diagram of the contact point between the jet flow and the pavement.

shoots to the pavement at a certain angle, so the position of the contact point can be obtained through theoretical calculation, and the calculation formula is eq.16.

$$L = H / \tan \theta \qquad (16)$$

where, L is the horizontal distance between the contact point and the engine nozzle, m; θ is the installation angle of aircraft engine, °; H is the height of the engine nozzle, m.

In order to accurately find the contact point between the jet flow and the pavement, the infrared thermometer was used for auxiliary measurement. Through measurement, we preliminarily determined that the highest temperature was located on the axis of the measurement area 16m away from the engine nozzle along the Z axis. After measurement, we preliminarily determined that the highest temperature was located on the axis of the measurement area 16m away from the engine nozzle. After obtaining the contact points of airflow and pavement, the field measurement points were arranged. In this experiment, 14 measurement points were set up for embedding temperature sensors. Symmetrical layout is adopted, and the measurement points were arranged by encryption in the

central area. The specific layout scheme is shown in Fig.10. Among them, Measuring points 7, 8 and 9 are located in the same position, which are 16m away from the engine nozzle along the Z axis on the axis of the pavement, but the buried depth is different., and measurement point 7 was buried 2mm below the pavement surface, measurement point 8 was buried 1cm below the pavement surface, and measurement point 9 was buried 2cm below the pavement surface. Measuring points 3 and 4 are located in the same position, both of which are 15m away from the engine nozzle along the Z axis on the axis of the pavement, but the buried depth is different. The measuring point 3 was buried 2mm below the pavement surface, and the measuring point 4 was buried 1cm below the pavement surface. Other measurement points were buried 2mm below the pavement surface, and the data acquisition device is located on the side of the concrete slab.

C. EXPERIMENTAL MEASUREMENT

In the experiment, the aircraft engine was in the state of full afterforce (see Fig.11). The temperature changes at each measuring point under the action of jet flow were recorded with 12 seconds as the time interval. After the temperature at each measuring point became stable, the experiment was finished. Two groups of experiments were conducted, and the average of the pavement temperature at each time in the two experiments was taken as the final data of the pavement temperature.Specific experimental procedures are as follows:

(1) Adjust aircraft attitude and fix the aircraft before test.Start the engine and heat the pavement with the jet flow;

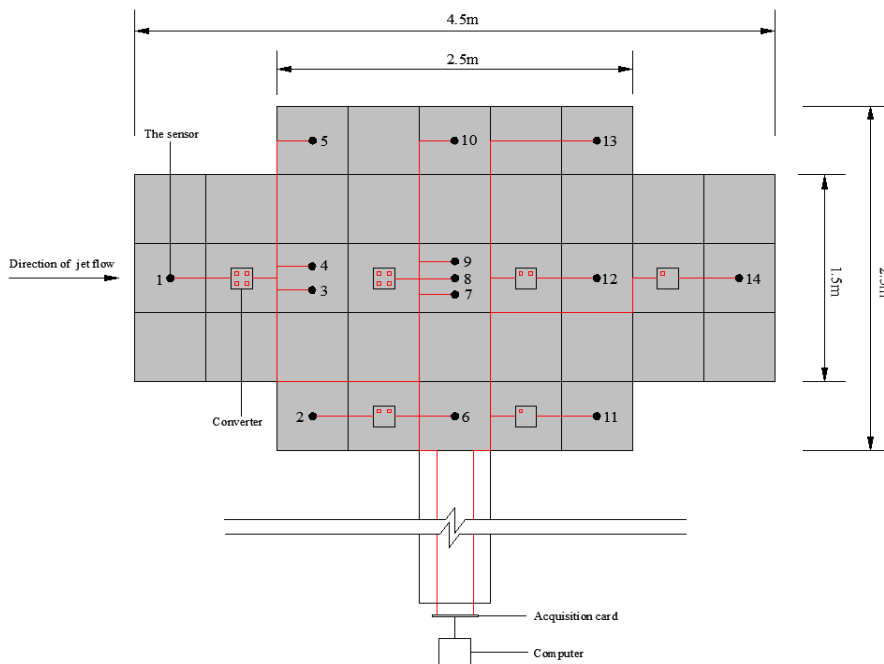(2) On the basis of theoretical calculation, an infrared thermometer is used to further determine the precise contact

FIGURE 10. Schematic diagram of measurement point layout.

IEEE *Access*

Z. Chen *et al.*: Simulation and Experimental Analysis of the Temperature Field of Jet Flow of Aircraft Based on CFD Theory

TABLE 3. Maximum temperature at rach measuring point under the condition of full afterload of aircraft engine (K).

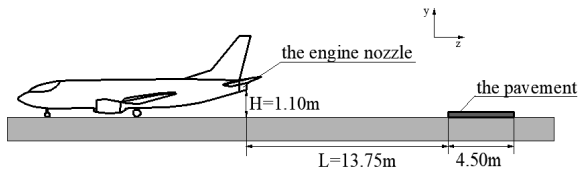| Measuring point	1	2	3	4	5	6	7
The experimental value	356.32	360.83	367.86	356.19	365.13	368.26	372.91
The simulation value	370.19	362.59	373.96		361.12	365.41	376.81
Measuring point	8	9	10	11	12	13	14
The experimental value	359.24	356.22	367.85	298.87	370.25	362.26	367.34
The simulation value			365.79	361.19	375.92	360.24	373.49

FIGURE 11. Schematic diagram of the interaction between aircraft and pavement.

point between the jet flow and the pavement, and then the aircraft engine is shut down;

(3) With the contact point between the jet flow and the pavement as the center, lay out the concrete slab as shown in figure 10. Connecting sensors, temperature converters and data acquisition devices, debugging instruments;

(4) After the preparation, start the aircraft engine again to the state of full afterforce, measure and collect data after the engine is running steadily. When the pavement temperature becomes stable, the experiment is finished.

D. ANALYSIS OF EXPERIMENTAL RESULTS

At the end of the experiment, the data collected by the data acquisition devices were sorted out and summarized. Taking the measuring point 7 as an example, the change of pavement temperature during the experiment was analyzed (see Fig.12). The pavement temperature increased rapidly before 120s, and when it reached 240s, the temperature tended to be stable (see Fig.12). It can be considered that the pavement temperature had reached the maximum value. On this basis, the maximum temperature of each measurement point during the experiment was statistically calculated (see Table 3).

By analyzing table 1, it can be concluded that:

1) Among the 14 groups of data, the data obtained from the measurement point 11 deviated greatly from the theoretical value. The reason is that there is a problem with the temperature sensor, so this set of data is invalid, and the other 13 sets of data are valid.

2) As can be seen from the table, the temperature at the measurement point 7 (that is, the contact point between the jet flow and the pavement) was the highest, at 372.91K. The lowest temperature at the measuring point 4 is 356.19K.

3) With measuring point 7 as the center, the temperature shows a symmetrical decrease trend along the transverse direction. Along the axis, there is also a decreasing trend, but the temperature variation rules are different in the
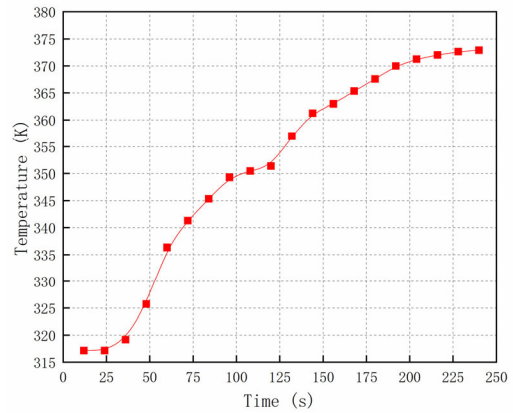

FIGURE 12. Temperature-time curve at measuring point 7.

two directions. The pavement temperature far away from the nozzle direction of the engine was significantly higher than that near the nozzle direction of the engine, indicating that the forward jet flow of the engine had a greater influence on the pavement temperature change.

4) Compare and analyze the pavement temperature obtained at measurement point 7, 8 and 9. Besides, the pavement temperature obtained by measuring point 3 and 4 was compared and analyzed. It can be found that the influence of jet flow on pavement temperature decreases with the increase of depth.

IV. COMPARATIVE ANALASIS

A. COMPARATIVE ANALYSIS OF RESULTS

The results of field experiment and numerical simulation are compared and analyzed. The pavement temperature at the distance from the nozzle Z=15.00m, 16.00m, 17.00m, 18.00m are extracted from simulaton and experiment (see Fig.13).

It can be concluded from the analysis of Fig.12 that:

1) On the axis of the pavement, the pavement temperature obtained by simulation and measurement experiment presents the same variation trend. Both show the rule of increasing first and then decreasing, and the maximum temperature point of both is 16m away from the nozzle along the Z axis. In comparison, the maximum temperature point measured by experiment is closer to the engine nozzle than the maximum temperature point calculated by simulation.

2) The simulation value is larger than the experiment value on the whole. Within the range of the figure, when
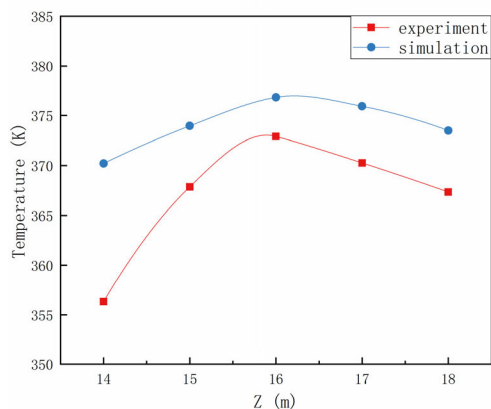
Z. Chen *et al.*: Simulation and Experimental Analysis of the Temperature Field of Jet Flow of Aircraft Based on CFD Theory

IEEE *Access*

FIGURE 13. Comparison diagram of pavement temperature simulation value and experimental test value.

located 14m away from the nozzle along the Z axis, the temperature difference between the two is the largest, 13.87K; when located 16m away from the nozzle along the Z axis, the temperature difference between the two is the smallest, 3.9K. and the average difference is 7.14K. Analysis reason: the simulation condition is ideal, but the field experiment has the environment factor and the measurement error and so on disturbance factor. Moreover, the simulation results correspond to the temperature of the pavement surface, while the temperature collected by the sensor in the experiment is 2mm deep in the pavement surface. Therefore, it is a normal phenomenon that the result obtained by the simulation calculation is larger than the result obtained by the field experiment.

3) As can be seen from the figure, when the distance from the nozzle is less than 16m, the variation trend of pavement temperature with distance measured by experiment is larger than that calculated by simulation. When the distance from the nozzle is larger than 16m, there was little difference in the variation trend between the two.In addition, the pavement temperature far away from the nozzle direction of the engine was significantly higher than that near the nozzle direction of the engine both in experiment and simulation.

B. SIMULATION MODEL CALIBRATE

In order to verify the accuracy of the simulation model, the t-test method was adopted: pairwise two-sample analysis of the mean value. In view of the significant problems in the experimental data of measuring point 11, the simulation and experimental values of measuring point 1, measuring point 2, measuring point 3, measuring point 5, measuring point 6, measuring point 7, measuring point 10, measuring point 12, measuring point 13 and measuring point 14 (see Table 3) were selected as the verification data to calibrate the simulation results. The test method formula is equation (17).

$$T = \frac{\bar{Y} - \mu_0}{S^*/\sqrt{n}}, \bar{Y} = \frac{1}{n}\sum_{i=1}^{n}Y_i, S^* = \sqrt{\frac{1}{n-1}\sum_{i=1}^{n}\left(Y_i - \bar{Y}\right)^2}$$

(17)

Use X_1 and X_2 to represent the simulated value and experimental value respectively, and take $Y = X_1 - X_2$. According to the theorem of large Numbers, Y obeys the normal distribution, that is, $Y \sim N\left(\mu, \sigma^2\right)$. The difference test between the experimental value and the simulated value is transformed into a hypothesis test to test the mean of the sample in mathematical statistics. According to the characteristics of the data in this paper, hypothesis $\mu = 0$ is proposed.

After calculation, the following results can be obtained:

$$\bar{Y} = 2.65, \quad S^* = 3.82$$

Take the confidence level $\alpha = 0.01$ and query the table of unilateral critical values of t distribution to get:

$$t_{\alpha/2}(n-1) = t_{0.005}(9) = 3.25$$

The following results are obtained:

$$t_1 = \frac{\bar{Y} - \mu_0}{S^*/\sqrt{5}} = 1.96 < 3.25$$

Therefore, when the confidence is 0.01, it can be assumed that there is no significant difference between the simulation value and the experimental value. Through the above analysis, it can be concluded that the simulation result of the pavement temperature distribution is basically consistent with that of the field measurement experiment.By means of mathematical test, the numerical difference between the two is very small, which verifies the accuracy of the numerical simulation model of pavement temperature field distribution under the action of the jet flow.

V. CALCULATION OF THE MAXIMUM TEMPERATURE OF THE PAVEMENT

The comparison and analysis between the numerical simulation results of type A aircraft and the field test results confirm that the numerical simulation model of pavement temperature distribution established by CFD theory is consistent with actual pavement temperature distribution. The accuracy difference of the model is within the allowable range of engineering, so the model can be utilized to simulation experiments.Therefore, this model is utilized to simulate the commonly used type B aircraft and type C aircraft.

A. SIMULATION ANALYSIS OF THE FULL AFTERFORCE STATE OF TYPE B AIRCRAFT

Type B aircraft is actually equipped with two engines. However, considering that the aircraft is still in the state of single engine during the preflight detection, this simulation model is still used for the simulation calculation of type B aircraft.The simplified model of the engine nozzle of type B aircraft is shown in Fig.14. Nozzle type of type B aircraft is the same as that of type A aircraft, both of which belong to convergent tubes, but the engine parameters are different. Type B aircraft engine nozzle diameter is 0.52m and the lowest point of nozzle is 1.43m above the ground.When the engine is working, the total temperature is 1279.15K, the static temperature

IEEE Access

Z. Chen *et al.*: Simulation and Experimental Analysis of the Temperature Field of Jet Flow of Aircraft Based on CFD Theory

TABLE 4. Comparison table of pavement temperature distribution under the action of jet flow of aircraft (K).

Type	Distance from nozzle Z（m）									
	6	8	10	12	14	16	18	20	22	24
type A aircraft	300.25	338.07	358.12	362.45	370.19	376.81	373.49	371.46	369.72	367.95
type B aircraft	310.49	395.42	460.90	493.77	509.56	516.10	516.77	514.60	510.73	504.71
type C aircraft	298.14	336.38	407.45	461.47	496.08	516.41	527.41	532.49	533.81	531.79

Note: the data in the table is the pavement temperature of X=0.
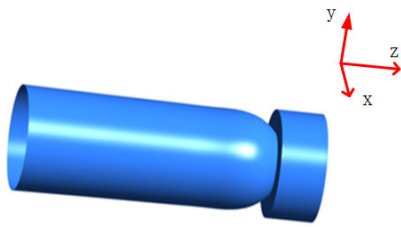

FIGURE 14. Geometric model of type B aircraft engine nozzle.

FIGURE 15. Cloud diagram of pavement temperature distribution under the action of type B aircraft.

is 1137.15K, and the airflow velocity at the outlet of the nozzle is 574m/s.

Under the action of jet flow of type B aircraft, the cloud diagram of airflow temperature on the pavement is shown in Fig.15. As can be observed in the figure, the pavement temperature increases first and then decreases along the axial direction, and decreases symmetrically along the transverse direction. Compared with the pavement temperature cloud diagram of type A aircraft, the pavement temperature of both of them start to rise from 6m away from the engine nozzle. However, the position of the core high temperature zone of type B aircraft is slightly moved forward compared with that of type A aircraft. The maximum temperature of type B aircraft is higher than that of type A aircraft significantly, and it remains at a higher temperature for a longer distance along the forward direction of the jet flow.

B. SIMULATION ANALYSIS OF THE FULL AFTERFORCE STATE OF TYPE C AIRCRAFT

In the same step, we use this model to simulate the temperature field distribution with the action of the jet flow from type C aircraft. Type C aircraft is a supersonic aircraft with high engine power and low installation altitude.The diameter of the engine nozzle is 0.44-0.46m and the lowest point of the nozzle is 0.60m above the ground.When the engine is working, the total temperature is 1233.15K, the static temperature is 1097.15K, and the airflow velocity at the outlet of the nozzle is 561m/s. The engine nozzle is laval nozzle, and the throat area changes can realize different working states. The simplified model of the nozzle is illustrated in Fig.16.

Through simulation calculation, the temperature distribution cloud diagram of the pavement under the action of jet flow from type C aircraft was obtained (see Fig.17).
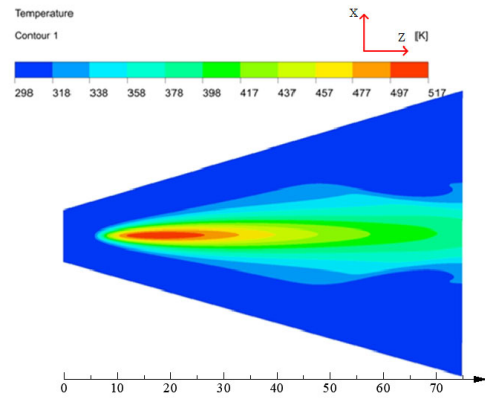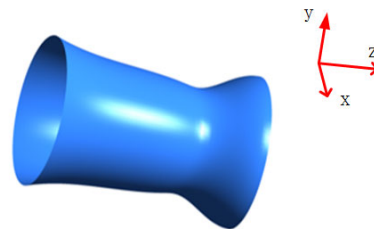

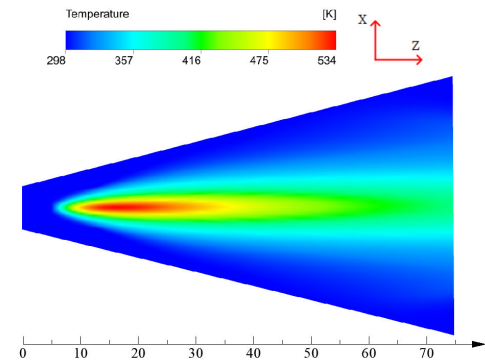**FIGURE 16.** Geometric model of type C aircraft engine nozzle.

FIGURE 17. Cloud diagram of pavement temperature distribution under the action of type C aircraft.

According to the analysis, the pavement temperature distribution under the action of type C aircraft is the same as that of type B aircraft and type A aircraft, both of which
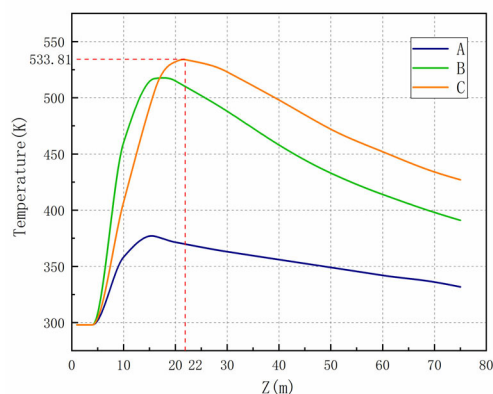
Z. Chen *et al.*: Simulation and Experimental Analysis of the Temperature Field of Jet Flow of Aircraft Based on CFD Theory

IEEE*Access*

FIGURE 18. Contrast diagram of the pavement temperature under the action of three jet flows.

show a trend of decreasing transverse symmetry, first increasing and then decreasing axial direction. The difference is that the maximum temperature in the core area of type C aircraft is higher than that of type A aircraft and type B aircraft, but the temperature change speed is not as high as that of type B aircraft. The initial heating position of type C aircraft was moved forward. The reason was analyzed, which was caused by the reduction of the engine installation height and the forward movement of the contact point between the jet flow and the pavement. Compared with type A aircraft and type B aircraft, the area of high-temperature area under the action of type C aircraft is still further increased.

C. ANALYSIS OF THE MOST ADVERSE SITUATION OF PAVEMENT TEMPERATURE DISTRIBUTION

Through the analysis of the pavement temperature cloud diagram generated under the action of the three types aircraft, the temperature situation of the pavement at different positions was statistically calculated (see Table 4). The surface temperature distribution under the action of three kinds of jet flow is plotted (see Fig. 18). As can be seen from the table and the figure, in the jet flow of three types of aircraft, the surface temperature increases first and then decreases as the distance from the nozzle increases along the z-axis. Under the action of type A aircraft, the surface temperature reaches a maximum of 376.81K at a distance of 16m from the nozzle. Under the action of type B aircraft, at the distance of 18m from the nozzle, the surface temperature reaches a maximum of 516.77K. Under the action of type C aircraft, the surface temperature reaches the maximum at 22m away from the nozzle, which is 533.81K. In terms of the maximum temperature, the maximum temperature of the pavement under the action of type C aircraft is the highest, followed by type B aircraft, and type A aircraft is the smallest. As for the change trend of pavement temperature, the pavement temperature increases the fastest with the increase of distance under the action of type B aircraft, followed by type C aircraft, and type A aircraft is the slowest.

VI. CONCLUSION

In this paper, the temperature field distribution of the pavement under the action of jet flow from the aircraft engine is studied, which provides the basis for the research on the adaptability of fiber concrete in the field of airport pavement and the durability of pavement material. A method combining numerical simulation with field measurement is proposed. Based on CFD theory, a numerical simulation model of the surface temperature distribution of type A aircraft under the action of jet flow is established. Field measurement experiments are carried out with the aid of temperature sensor to verify the accuracy of the simulation model. On this basis, numerical simulation was carried out for the other two commonly used aircraft, and the ultimate temperature of the runway under the action of the tail jet flow was calculated to be 533.51K. Therefore, if fiber concrete is to be popularized in the field of airport pavement, it is necessary to verify whether it can maintain sufficient durability under such conditions.

In this paper, field measurement method and numerical simulation are combined to ensure the measurement accuracy while greatly reducing the cost of field measurement, giving full play to the advantages of the two research methods. The research in this paper is of guiding significance to the measurement of physical properties and the study of mechanical properties of airport pavement and can be applied in other fields of pavement properties research.

At present, the research only stays at the level of pavement temperature field distribution. In the next step, the durability and high temperature resistance of fiber concrete will be studied to verify the reliability of the application of fiber concrete in the field of airport pavement. In addition, simulation research will be carried out for more aircraft, and the combination of wireless temperature sensor and communication technology will be considered to realize real-time measurement of pavement temperature field.

CONFLICT OF INTEREST

The author declares no conflict of interest regarding the publication of this paper.

REFERENCES

[1] (May 2019). *The 2018 Statistical Bulletin on the Development of China's Civil Aviation Industry*. [Online]. Available: https://http://www.caac.gov.cn/XXGK/XXGK/TJSJ/201905/t20190508_196033.html

[2] R. Talikoti and S. Kandekar, "Strength and durability study of concrete structures using aramid-fiber-reinforced polymer," *Fibers*, vol. 7, no. 2, pp. 1–11, 2019.

[3] J. Liu, Y. Jia, and J. Wang, "Experimental study on mechanical and durability properties of glass and polypropylene fiber reinforced concrete," *Fibers Polymers.*, vol. 20, no. 9, pp. 1900–1908, 2019.

[4] Y. Chen, G. Cen, and Y. Cui, "Comparative study on the effect of synthetic fiber on the preparation and durability of airport pavement concrete," *Construct. Building Mater.*, vol. 184, pp. 34–44, Sep. 2018.

[5] Z.-W. Wang, D.-Y. Yang, C. Ge, Y.-S. Li, and J.-F. Lv, "Properties of steel fiber reinforced concrete under thermal-force coupling," *Bull. Chin. Ceramic Soc.*, vol. 38, no. 6, pp. 3490–3497, 2019.

[6] A. Loizos, C. Plati, and V. Papavasiliou, "Fiber optic sensors for assessing strains in cold in-place recycled pavements," *Int. J. Pavement Eng.*, vol. 14, no. 2, pp. 125–133, Feb. 2013.

IEEE *Access*

Z. Chen *et al.*: Simulation and Experimental Analysis of the Temperature Field of Jet Flow of Aircraft Based on CFD Theory

[7] H. Yan, W. Zhang, and D. Wang, "Wheel force sensor-based techniques for wear detection and analysis of a special road," *Sensors*, vol. 18, no. 8, pp. 2493–2505, 2018.

[8] H. Zhao, D. Wu, M. Zeng, and J. Ling, "Support conditions assessment of concrete pavement slab using distributed optical fiber sensor," *Transportmetrica A, Transp. Sci.*, vol. 15, no. 1, pp. 71–90, Feb. 2019.

[9] J. Godoy, R. Haber, J. Muñoz, F. Matía, and Á. García, "Smart sensing of pavement temperature based on low-cost sensors and V2I communications," *Sensors*, vol. 18, no. 7, p. 2092, 2018.

[10] B. B. Teltayev and E. A. Suppes, "Temperature in pavement and subgrade and its effect on moisture," *Case Stud. Thermal Eng.*, vol. 13, Mar. 2019, Art. no. 100363.

[11] S. Cai, H. Yuan, Y. Cui, B. Tian, and J. Lv, "An ISO/IEC/IEEE21451 smart sensor network for distributed measurement of pavement structural temperature," *Int. J. Distrib. Sensor Netw.*, vol. 12, no. 3, Mar. 2016, Art. no. 3408489.

[12] J. D. Anderson, *Computational Fluid Dynamics*. New York, NY, USA: McGraw-Hill, 1995.

[13] D. Caughey and M. Hafez, *Frontiers of Computational Fluid Dynamics*, Singapore: World Scientific, 2005.

[14] H. F. Wang, L. C. Cai, X. L. Chong, and H. Geng "Experimental study of the jet engine exhaust flow field of aircraft and blast fences," *Promet-Traffic Transp.*, vol. 27, no. 2, pp. 181–190, 2015.

[15] L. A. Benderskiy, D. A. Lyubimov, and A. O. Chestnykh, "Numerical investigation on the interaction of a pair of hot off-design supersonic jets with a jet blast deflector," *TsAGI Sci. J.*, vol. 49, no. 1, pp. 13–28, 2018.

[16] L. A. Benderskii, D. A. Lyubimov, A. O. Chestnykh, B. M. Shabanov, and A. A. Rubakov, "The use of the RANS/ILES method to study the influence of coflow wind on the flow in a hot, nonisobaric, supersonic airdrome jet during its interaction with the jet blast deflector," *High Temp.*, vol. 56, no. 2, pp. 247–254, Mar. 2018.

[17] K. Yue, L. Cheng, H. Liu, and Y. Wang, "Analysis of jet blast impact of embarked aircraft on deck takeoff zone," *Aerosp. Sci. Technol.*, vol. 45, pp. 60–66, Sep. 2015.

[18] K. Yue, Y. Sun, H. Liu, and W. Guo, "Analysis of the flow field of carrier-based aircraft exhaust jets impact on the flight deck," *Int. J. Aeronaut. Space Sci.*, vol. 16, no. 1, pp. 1–7, Mar. 2015.

[19] M. Song, J.-G. Tan, X.-K. Li, and J. Hao, "The effect analysis of an engine jet on an aircraft blast deflector," *Trans. Inst. Meas. Control*, vol. 41, no. 4, pp. 990–1001, 2018.

[20] J. Liu, A. Corrigan, K. Kailasanath, R. Ramamurti, N. Heeb, D. Munday, and E. Gutmark, "Impact of deck and jet blast deflector on the flow and acoustic properties of an imperfectly expanded supersonic jet," *Nav. Eng. J.*, vol. 127, no. 3, pp. 47–60, 2013.

[21] J. Liu, K. Kailasanath, N. Heeb, D. Munday, and E. Gutmark, "Large-eddy simulations of a supersonic heated jet," in *Proc. 17th AIAA/CEAS Aeroacoustics Conf., 32nd AIAA Aeroacoustics Conf.*, Jun. 2011, pp. 2884–2909.

[22] T. Sun, T. H. Xiao, X. Mu, X. Li, and Y. C. Zhang, "Studies on CFD based deck flow field modeling of carrier-borne aircraft flight simulator," *J. Syst. Simul.*, vol. 25, no. 8, pp. 82–85, 2013.

[23] H. Feng, Z. H. Yao, and J. S. Xie, "Numerical simulation of flow field of three-dimensional sonic impinging jet," *Propuls. Technol.*, vol. 25, no. 1, pp. 16–19, 2002.
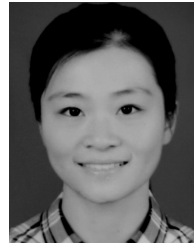
WANTONG CAI received the B.S., M.S., and Ph.D. degrees in airport engineering from Air Force Engineering University, Xi'an, China, in 2012, 2014, and 2018, respectively.

Her research interests include pavement materials, and airport pavement design and evaluation.

LIANGCAI CAI received the B.S. and M.S. degrees in airport engineering from Air Force Engineering University, Xi'an, China, in 1984 and 1987, respectively, and the Ph.D. degree in road and railway engineering from Southeast University, in 1995.

He is currently a Professor with the Department of Airport Engineering and Architecture, Air Force Engineering University, China. His research interests include planning and management of airport, environmental protection and evaluation of airport, and airport pavement design.
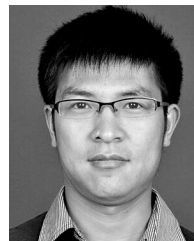
GUOPING CEN received the B.S. and M.S. degrees in airport engineering from Air Force Engineering University, Xi'an, China, in 1984 and 1987, respectively, and the Ph.D. degree in road and railway engineering from Hohai University, in 1995.

He is currently a Professor with the Department of Airport Engineering and Architecture, Air Force Engineering University, China. His research interests include planning and management of airport, airport pavement design, and airport drainage design.
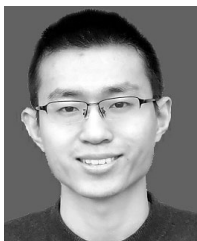
ZHENGLEI CHEN received the B.S. degree in airport engineering from Air Force Engineering University, Xi'an, China, in 2018, where he is currently pursuing the M.S. degree in airport engineering.

His research interests include planning and management of airport, and planning and design of airport apron.

HAIFU WANG received the B.S., M.S., and Ph.D. degrees in airport engineering from Air Force Engineering University, Xi'an, China, in 2011, 2013, and 2017, respectively.

His research interests include simulation and jet blast deflector.

• • •